Effect of underground cavities on surface earthquake ground motion under SH wave propagation

ARTICLE *in* EARTHQUAKE ENGINEERING & STRUCTURAL DYNAMICS · OCTOBER 2009

Impact Factor: 2.31 · DOI: 10.1002/eqe.912

4 AUTHORS, INCLUDING:

Chiara Smerzini
Politecnico di Milano
26 PUBLICATIONS **237** CITATIONS
SEE PROFILE

Roberto Paolucci
Politecnico di Milano
100 PUBLICATIONS **1,654** CITATIONS
SEE PROFILE

EARTHQUAKE ENGINEERING AND STRUCTURAL DYNAMICS
Earthquake Engng Struct. Dyn. 2009; **38**:1441–1460
Published online 5 March 2009 in Wiley InterScience (www.interscience.wiley.com). DOI: 10.1002/eqe.912

Effect of underground cavities on surface earthquake ground motion under SH wave propagation

C. Smerzini[1,*,†], J. Avilés[2], R. Paolucci[3] and F. J. Sánchez-Sesma[4]

[1]*Doctoral School of Earthquake Engineering and Engineering Seismology, ROSE School, IUSS Pavia, Via Ferrata 1, 27100, Pavia, Italy*
[2]*Instituto Mexicano de Tecnología del Agua IMTA, México*
[3]*Department of Structural Engineering, Politecnico di Milano, P.za Leonardo da Vinci 32, 20133, Milano, Italy*
[4]*Instituto de Ingeniería, Universidad Nacional Autónoma de México UNAM, Cd. Universitaria, Circuito Escolar s/n, Coyoacán 04510, México D. F., Mexico*

SUMMARY

A theoretical approach is presented to study the antiplane seismic response of underground structures, subjected to the incidence of both plane and cylindrical waves. The structure is assumed to be a circular inclusion embedded in a homogenous, isotropic and linear visco-elastic halfspace. The inclusion may consist either of a cavity, with or without a ring-shaped boundary, or it may be filled in with a linear-elastic material, without loss of generality. The analytical solution is obtained using expansions of wave functions in terms of Bessel and Hankel functions, relying on the technique of images and the use of Graf's addition theorem to enforce the boundary conditions.

The effects of underground cavities on surface earthquake ground motion are studied as a function of the size of the cavity, its embedment depth, the frequency content of the excitation, the incidence angle and the distance from the axis of symmetry of the cavity itself. A simple application of Rayleigh's method allows us to verify that the ground surface response is dominated by the fundamental vibration mode of the portion of soil between the cavity and ground surface itself, in the frequency range of interest for engineering purposes. A simple relationship to estimate the fundamental natural frequency as a function of the embedment depth of the cavity is given. Finally, amplification factors on response spectra are obtained, to provide a practical insight into the effect of an underground cavity on surface ground motion during real earthquakes. Copyright © 2009 John Wiley & Sons, Ltd.

Received 10 November 2008; Revised 8 January 2009; Accepted 27 January 2009

KEY WORDS: analytical solution for SH wave propagation; underground cavities; Rayleigh's method; spectral amplification factors

*Correspondence to: C. Smerzini, Doctoral School of Earthquake Engineering and Engineering Seismology, ROSE School, IUSS Pavia, Via Ferrata 1, 27100, Pavia, Italy.
†E-mail: csmerzini@roseschool.it

Contract/grant sponsor: DGAPA-UNAM; contract/grant number: IN114706

INTRODUCTION

It is widely recognized that significant earthquake ground motion amplifications may occur due to the presence of either surface or subsurface irregularities. While numerous studies have been developed on the effects induced by valleys and topographies, and implemented in seismic norms as well (see e.g. Part 5 of Eurocode 8 [1]), understanding and quantifying the effects of underground irregularities, such as buried cavities or tunnels, is still at a research stage. Similarly, the identification and characterization of either natural or artificial subsurface obstacles, such as cavities or petroleum reservoirs, constitute a challenging issue for geophysical subsurface investigations.

In their pioneering work, Pao and Mow [2] studied the diffraction of SH elastic waves and dynamic stress concentration by a circular cylinder embedded in an ideal infinite space. Later, other authors [3, 4] considered the scattering of elastic waves by a cylindrical cavity in a semi-infinite medium. Dravinski [5, 6] presented a detailed literature review on the scattering of elastic waves by subsurface irregularities, while Lee and co-workers undertook a systematic study to analyze, first, the scattered wavefield induced by either a cavity or a tunnel under plane SH waves incidence [7, 8], and, secondly to generalize it to 3D elastic diffraction [9], and to SV and P incidence [10, 11]. Finally, the interaction effects between surface (e.g. canyon or valley) and subsurface cavities/tunnels and their influence on surface ground motion were studied in [12].

The first objective of this paper is to provide a comprehensive analytical framework to assess the modification of seismic surface ground motion due to underground inclusions, capable of considering the incidence of both plane and cylindrical SH waves. The problem is formulated by modelling the cross-section of the subsurface irregularities as an ideal circular inclusion embedded in a homogenous, isotropic and linear visco-elastic halfspace. The method of solution, first introduced by Avilés and Mora-Orozco [13], starts by defining a suitable set of cylindrical coordinates. In each reference system, the diffracted or refracted wavefield is represented by means of the method of separation of variables, in terms of series of Bessel and Hankel functions. The enforcement of the boundary conditions, made possible with the aid of the Graf's addition theorem [14], allows us to obtain the exact solution. The solution technique is similar to the one proposed by Lee and Trifunac [8], Avilés and Sánchez-Sesma [15] and Lee *et al.* [12]. Nevertheless, contrary to the previous works, this method of solution is versatile enough to deal not only with various kinds of buried obstacles, from cavities to elastic inclusions, but also different types of excitations. Referring to the latter point, an exact asymptotic equivalence between the response under incident plane and cylindrical waves is demonstrated relying upon a suitable normalization technique.

The second objective is to provide quantitative estimates of the seismic amplification of surface ground motion above underground cavities. As far as available from literature, while several closed-form solutions for the dynamic response of embedded cavity have been proposed in the last 30 years (see e.g. [8, 16]), only a very limited effort has been devoted so far to translate the theoretical findings in a format useful for engineering applications.

The work is organized as follows. We first present the mathematical model for plane SH waves impinging on an circular inclusion and, secondly, generalize the method to the case of a point source of cylindrical waves. Some representative numerical results are then presented in a parametric way both in time and frequency domains, showing their dependence on the type of inclusion (cavity, tunnel or elastic inclusion), its embedment depth, the frequency content of the input wavefield and the distance of the observation point from the axis of symmetry. Finally, after providing the physical interpretation of the peaks of the transfer functions of surface ground motion above underground

DOI: 10.1002/eqe

cavities, relying on a simple application of Rayleigh's method, response spectral amplification factors are calibrated and illustrated for some realistic sets of parameters.

MATHEMATICAL MODEL

The mathematical model is depicted in Figure 1. It consists of a cylindrical inclusion with circular cross-section of radius a_c embedded in a homogenous, isotropic and linear visco-elastic halfspace. The inclusion may be either internally empty (cavity), or filled in with a linear visco-elastic material (elastic inclusion), or its cross-section may include a ring-shaped boundary of variable thickness with different elastic properties from the halfspace (lined tunnel), as sketched in Figure 1(a). According to the notation used in Figure 1, the halfspace will be denoted by index S, while the interior region of the buried structure by C. Two reference systems are superimposed in Figure 1, the former located on the free surface and at distance L from the center of the inclusion, and the latter centered in the inclusion itself at depth H. The incident wavefield undergoes phenomena of multiple scattering and diffraction owing both to the free surface and to the presence of the inclusion. Under the assumption of incidence SH plane waves, the total displacement wavefield in the halfspace w_s is a scalar quantity and has to satisfy the reduced wave equation, i.e. Helmholtz equation [17]:

$$\nabla^2 w_s + k_s^2 w_s = 0 \quad \text{with } \nabla^2 = \frac{\partial^2}{\partial^2 x} + \frac{\partial^2}{\partial^2 y} \tag{1}$$

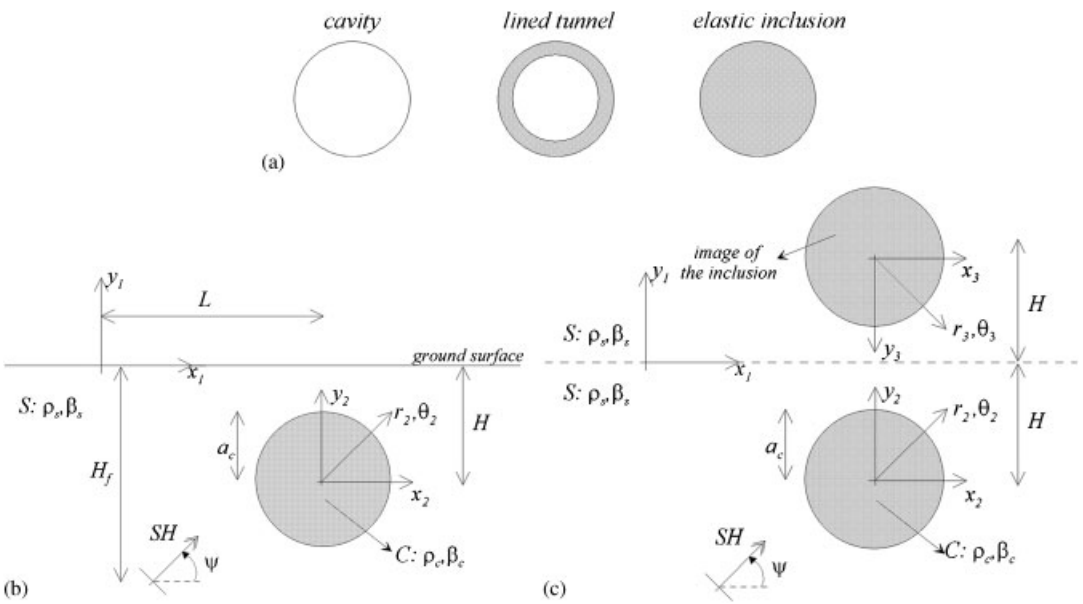

Figure 1. (a) Various buried structures considered in this work; (b) sketch of the mathematical model; and (c) method of images.

DOI: 10.1002/eqe

where $\beta_s = \sqrt{\mu_s/\rho_s}$ is the complex shear wave velocity of the halfspace with mass density, shear modulus and quality factor given by ρ_c, μ_c and Q, respectively, and $k_s = \omega/\beta_s$ is the wavenumber associated with shear waves.

Relying on the theory of elastic wave diffraction [2], the wavefield w_s within the halfspace results from the superposition of the free-field $w^{(0)} = w^{(i)} + w^{(r)}$ given by the incident and reflected wavefields in the absence of the anomaly C, of the wavefield $w_f^{(d)}$ diffracted by the surface of the obstacle and of the wavefield $w_i^{(d)}$ diffracted by the surface of the image of the inclusion (see sketch in Figure 1(c)), as follows:

$$w_s = w^{(i)} + w^{(r)} + w_f^{(d)} + w_i^{(d)} \tag{2}$$

If the incident wavefield is represented by a train of SH plane waves, polarized in the z direction, the free-field $w^{(0)}$ is given by the following expression:

$$w^{(0)} = w^{(i)} + w^{(r)} = 2e^{-ik_s x_1 \cos\psi} \cos(k_s y_1 \sin\psi) \quad \text{with } i = \sqrt{-1} \tag{3}$$

where ψ is the incidence angle. From here on, the time harmonic factor $e^{i\omega t}$ is understood and the wavefields are normalized with respect to the input displacement amplitude w_0. The diffracted fields induced by the inclusion and its image are obtained by solving Equation (1) with the method of separation of variables yielding:

$$w_f^{(d)} = \sum_{m=0}^{\infty} \{H_m^{(2)}(k_s r_2)[A_m \cos m\theta_2 + \hat{\delta}_{m0} B_m \sin m\theta_2]\} \tag{4}$$

and

$$w_i^{(d)} = \sum_{m=0}^{\infty} \{H_m^{(2)}(k_s r_3)[A_m \cos m\theta_3 + \hat{\delta}_{m0} B_m \sin m\theta_3]\} \tag{5}$$

where $H_m^{(2)}(\circ)$ is the Hankel's function of second kind and order m, while $\hat{\delta}_{m0} = 1$ for $m \neq 0$ and $\hat{\delta}_{m0} = 0$ for $m = 0$. The expansions of Equations (4) and (5) satisfy the stress-free condition at $y_1 = 0$ and the Sommerfeld radiation condition at infinity [18]. On the other hand, the displacement wavefield refracted and trapped within the inclusion can be expressed as follows:

$$w_c = \sum_{m=0}^{\infty} \{J_m(k_c r_2)[C_m \cos m\theta_2 + \hat{\delta}_{m0} D_m \sin m\theta_2]\} \tag{6}$$

where $k_c = \omega/\beta_c$ and $J_m(\circ)$ is the Bessel's function of first kind and order m.

The unknown coefficients A_m and B_m, as well as C_m and D_m, are determined by enforcing the boundary conditions regarding the continuity of displacements and stresses around the soil–inclusion interface:

$$w_s|_{r_2=a_c} = w_c|_{r_2=a_c} \quad \text{and} \quad \mu_s \left.\frac{\partial w_s}{\partial r_2}\right|_{r_2=a_c} = \mu_c \left.\frac{\partial w_c}{\partial r_2}\right|_{r_2=a_c} \quad \forall\theta_2 \in [0 \;\; 2\pi] \tag{7}$$

Note that C_m and D_m are not significant as we are mainly interested predominantly to reproduce the surface ground motion. Behind Equation (7) there is the assumption of a perfect bounding between the inclusion and the surrounding medium.

DOI: 10.1002/eqe

SOLUTION TECHNIQUE

The exact solution of the model is obtained by a boundary method which involves series expansion of incident and reflected SH waves in terms of cylindrical wave functions, as well as coordinate transformations between any two reference systems. To this end, it is convenient to express the total wavefield given by Equation (2) in terms of the polar coordinates (r_2, θ_2). First, the incident and reflected fields are expressed as series of cylindrical waves by means of the Neumann expansion [14], as follows:

$$w^{(\mathrm{i}),(\mathrm{r})} = \mathrm{e}^{\varphi^{(\mathrm{i}),(\mathrm{r})}} \mathrm{e}^{-\mathrm{i}k_S r_2 \cos(\theta_2 \mp \psi)} \quad \text{with } \varphi^{(\mathrm{i}),(\mathrm{r})} = -\mathrm{i}k_\mathrm{s}(L\cos\psi \mp H\sin\psi) \tag{8}$$

so that the free-field takes the form:

$$w^{(0)} = 2\mathrm{e}^{-\mathrm{i}k_\mathrm{s}L\cos\psi} \left\{ \cos(k_\mathrm{s}H\sin\psi) \sum_{m=0}^{\infty} [(-\mathrm{i})^m \varepsilon_m J_m(k_\mathrm{s}r_2)\cos m\psi \cos m\theta_2] \right.$$
$$\left. +2\mathrm{i}\sin(k_\mathrm{s}H\sin\psi) \sum_{m=1}^{\infty} [(-\mathrm{i})^m J_m(k_\mathrm{s}r_2)\sin m\psi \sin m\theta_2] \right\} \tag{9}$$

where ε_m is the Neumann factor ($\varepsilon_m = 1$ if $m = 0$, $\varepsilon_m = 2$ elsewhere). Note that the negative and positive signs in Equation (8) indicate the incident ($w^{(\mathrm{i})}$) and the reflected ($w^{(\mathrm{r})}$) wavefields respectively.

Finally, the diffracted wavefield $w_i^{(\mathrm{d})}$ can be expressed in terms of (r_2, θ_2) by Graf's addition theorem (see Appendix A for further details), leading to:

$$w_i^{(\mathrm{d})} = \sum_{m=0}^{\infty} \left\{ J_m(k_\mathrm{s}r_2) \left[\frac{\varepsilon_m}{2} \Lambda_{nm}^{+} \cos m\theta_2 + \hat{\delta}_{m0} \Lambda_{nm}^{-} \sin m\theta_2 \right] \right\} \tag{10}$$

with $\Lambda_{nm}^{\pm} = \sum_{n=0}^{\infty} (-1)^n [K_{nm}^{\pm} A_n \mp \hat{\delta}_{n0} L_{nm}^{\pm} B_n]$.

The transport factors $K_{nm}^{\pm}$ and $L_{nm}^{\pm}$, which directly arise from transferring the wave solution from system (r_3, θ_3) to (r_2, θ_2), are given by:

$$K_{nm}^{\pm} = \cos\left((n+m)\frac{\pi}{2}\right) H_{n+m}^{(2)}(2k_\mathrm{s}H) \pm (-1)^m \cos\left((n-m)\frac{\pi}{2}\right) H_{n-m}^{(2)}(2k_\mathrm{s}H) \tag{11a}$$

$$L_{nm}^{\pm} = \sin\left((n+m)\frac{\pi}{2}\right) H_{n+m}^{(2)}(2k_\mathrm{s}H) \pm (-1)^m \sin\left((n-m)\frac{\pi}{2}\right) H_{n-m}^{(2)}(2k_\mathrm{s}H) \tag{11b}$$

Appendix A provides details about a generalized version of the addition theorem, to transform wave functions from one reference system to another.

Solving system of equations

Substituting Equations (4), (9) and (10) into Equation (2), the total displacement wavefield is referred to the reference system (r_2, θ_2). By enforcing the boundary conditions (7) and taking into account the orthogonal properties of the trigonometric functions, we obtain four infinite linear systems of equations for the unknowns A_n, B_n, C_n and D_n. The field within the inclusion is of no

DOI: 10.1002/eqe

interest here and therefore C_n and D_n can be eliminated by substitution. The resulting system can then be written in matrix compact notation as follows:

$$\begin{bmatrix} G_{mn}^{11} & G_{mn}^{12} \\ G_{mn}^{21} & G_{mn}^{22} \end{bmatrix} \begin{Bmatrix} A_n \\ B_n \end{Bmatrix} = \begin{Bmatrix} I_m^1 \\ I_m^2 \end{Bmatrix} \tag{12}$$

where the independent terms $I_m^{1,2}$ are defined as:

$$I_m^1 = -4\cos(k_s H \sin\psi)\mathrm{e}^{-\mathrm{i}k_s L\cos\psi}(-\mathrm{i})^m \cos m\psi \tag{13a}$$

$$I_m^2 = -4\mathrm{i}\sin(k_s H \sin\psi)\mathrm{e}^{-\mathrm{i}k_s L\cos\psi}(-\mathrm{i})^m \sin m\psi \tag{13b}$$

The boundary conditions are those of continuity of displacements and tractions. It comes out, after solving the inclusion model, that the coefficients for the diffracted field admit simple limiting forms if the inclusion is a void or a lined tunnel. After some straightforward, but lengthy algebra, the sub-matrices G^{ij} can be expressed as:

$$\begin{aligned} G_{mn}^{11} &= (-1)^n K_{nm}^{+} + \frac{2}{\varepsilon_m}\delta_{mn}\Delta_m, \quad G_{mn}^{12} = -(-1)^n L_{nm}^{+} \\ G_{mn}^{21} &= (-1)^n L_{nm}^{-}, \quad G_{mn}^{22} = (-1)^n K_{nm}^{-} + \delta_{mn}\Delta_m \end{aligned} \tag{14}$$

where δ_{mn} is the Kronecker delta ($=1$ if $m=n$; $=0$ if $m\neq n$) while the factor Δ_m, which only affects the terms along the principal diagonal, is given by:

$$\Delta_m = \frac{H_m'^{(2)}(k_s a_c) - F_m H_m^{(2)}(k_s a_c)}{J_m'(k_s a_c) - F_m J_m(k_s a_c)} \tag{15}$$

where the prime denotes differentiation with respect to the argument and F_m is the inclusion factor defined as:

$$F_m = C\frac{J_m'(k_c a_c)}{J_m(k_c a_c)} \quad \text{with } C = \sqrt{\frac{\mu_c \rho_c}{\mu_s \rho_s}} \quad \text{for an elastic inclusion} \tag{16a}$$

$$F_m = C\frac{J_m'(k_c a_c) - \alpha_m Y_m'(k_c a_c)}{J_m(k_c a_c) - \alpha_m Y_m(k_c a_c)} \quad \text{with } \alpha_m = \frac{J_m'(k_c(1-b)a_c)}{Y_m'(k_c(1-b)a_c)} \quad \text{for a lined tunnel} \tag{16b}$$

$$F_m = 0 \quad \text{for a cavity} \tag{16c}$$

We end up with a well-structured system, straightforward to generalize not only to different kinds of buried inclusions of circular shape, but also to various incident wavefields (see the following section for further details). Note that in Equation (16b) $b=(a_c-a_i)/a_c$ is the dimensionless thickness of the wall of the tunnel, a_i and a_c being the inner and external radius, respectively, while $Y_m(\circ)$ is the Bessel's function of second kind and order m. Leaving aside its analytical derivation, Equation (16b) is obtained by imposing an additional boundary condition of vanishing shear strains at the inner boundary, i.e. $\partial w_c/\partial r_2|_{r_2=(1-b)a_c}$.

Infinite systems like in Equation (12) cannot in general be solved. Truncation to finite size is therefore necessary to obtain the solution at any point. In other words, the order of the expansions is set equal to M, such that the unknown coefficients are $2M+1$. Solutions were checked to be robust with respect to M; specifically, small values of M, typically around 6–10, are sufficient to obtain convergent solutions.

DOI: 10.1002/eqe

INCIDENCE OF CYLINDRICAL WAVES

In this section we illustrate how the solution technique, described previously for plane waves, can be generalized to incident cylindrical waves.

Similar to the plane wave case, we rely upon the method of images considering twin punctual sources in symmetrical position with respect to the free surface, as depicted in Figure 2. Note that two polar coordinate systems, (r_F, θ_F) and (r'_F, θ'_F), for the source and its image, respectively, are built up. Using Graf's addition theorem to pass from the polar coordinates, (r_F, θ_F) and (r'_F, θ'_F), to the reference system (r_2, θ_2), as sketched in Figure 2, we can derive the following expressions for the incident and reflected wavefields:

$$w^{\mathrm{i}}|_{cyl} = H_0^{(2)}(k_{\mathrm{s}} r_F) = \sum_{m=0}^{\infty} [\varepsilon_m (-1)^m H_m^{(2)}(k_{\mathrm{s}} R^i) J_m(k_{\mathrm{s}} r_2) \cos(m(\theta_2 - \psi^i))] \tag{17a}$$

$$w^{\mathrm{r}}|_{cyl} = H_0^{(2)}(k_{\mathrm{s}} r'_F) = \sum_{m=0}^{\infty} [\varepsilon_m (-1)^m H_m^{(2)}(k_{\mathrm{s}} R^r) J_m(k_{\mathrm{s}} r_2) \cos(m(\theta_2 + \psi^r))] \tag{17b}$$

where the geometrical quantities R^i, ψ^i, R^r and ψ^r are defined in Figure 2.

The strategy of solution consists in the normalization of Equation (17) with respect to the function $H_0^{(2)}(k_{\mathrm{s}} D)$, where the geometrical parameter D as the distance between the source and the reference system (x_1, y_1). Let us denote, for ease of notation, $H_m^{(2)}(k_{\mathrm{s}} R^i) = H_m^i$,

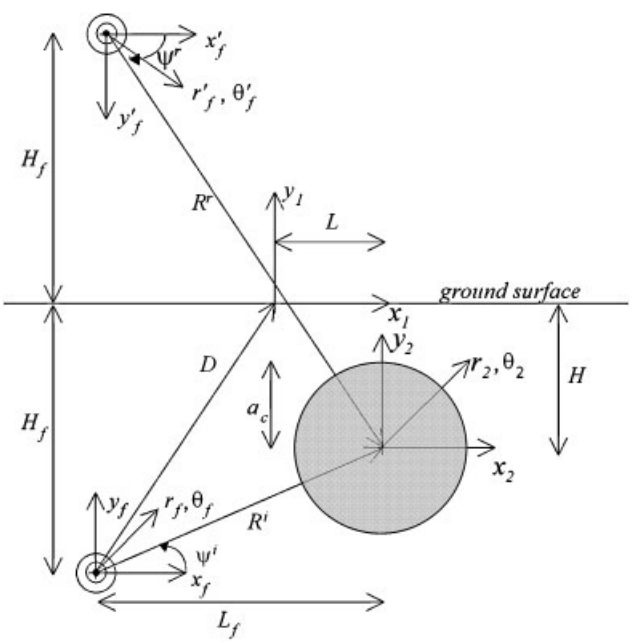

Figure 2. Sketch of the model to deal with cylindrical waves incidence.

DOI: 10.1002/eqe

$H_m^{(2)}(k_s R^r) = H_m^r$, $H_0^{(2)}(k_s D) = H_0^D$ and $J_m(k_s r_2) = J_m$. Therefore, we end up with a compact form for the cylindrical free-field:

$$w^{(0)}|_{cyl} = \frac{w^{\mathrm{i}}|_{cyl} + w^{\mathrm{r}}|_{cyl}}{H_0^D} = \frac{1}{H_0^D} \sum_{m=0}^{+\infty} \{\varepsilon_m (-1)^m J_m [a_m \cos m\theta_2 + b_m \sin m\theta_2]\} \tag{18}$$

with $a_m = H_m^i \cos m\psi^i + H_m^r \cos m\psi^r$ and $b_m = H_m^i \sin m\psi^i - H_m^r \sin m\psi^r$.

It is worth noticing that the system in Equation (12) can be generalized to the case of incidence represented by cylindrical waves, solely by changing the independent terms as follows:

$$I_m^1 = \frac{-2(-1)^m a_m}{H_0^D} \quad \text{and} \quad I_m^2 = \frac{-2(-1)^m b_m}{H_0^D} \tag{19}$$

The proposed normalization process allows one to establish an asymptotic equality between the free-field solution induced by plane waves and that induced by cylindrical waves in the limiting case for $D \to \infty$. Multiplying and dividing Equations (17a) and (17b) by H_0^i and H_0^r, respectively, we obtain:

$$w^{(0)}|_{cyl} = \frac{H_0^i}{H_0^D} \sum_{m=0}^{+\infty} \left[\varepsilon_m (-1)^m \frac{H_m^i}{H_0^i} J_m \cos m(\theta_2 - \psi^i) \right] + \frac{H_0^r}{H_0^D} \sum_{m=0}^{+\infty} \left[\varepsilon_m (-1)^m \frac{H_m^r}{H_0^r} J_m \cos m(\theta_2 + \psi^r) \right] \tag{20}$$

Using the asymptotic relations for the Hankel's functions [14] for $D \to \infty$ (implying that $R^i, R^r \to \infty$), we build up the following relations:

$$\frac{H_0^{i,r}}{H_0^D} \cong \frac{\sqrt{\dfrac{2}{\pi k_s R^{i,r}}}}{\sqrt{\dfrac{2}{\pi k_s D}}} \frac{\mathrm{e}^{-\mathrm{i}(k_s R^{i,r} - \pi/4)}}{\mathrm{e}^{-\mathrm{i}(k_s D - \pi/4)}} = \sqrt{\frac{D}{R^{i,r}}} \mathrm{e}^{-\mathrm{i}k_s (D - R^{i,r})} \tag{21}$$

and, similarly:

$$\frac{H_m^{i,r}}{H_0^{i,r}} \cong \frac{\mathrm{e}^{-\mathrm{i}(k_s R^{i,r} - m\pi/2 - \pi/4)}}{\mathrm{e}^{-\mathrm{i}(k_s D - \pi/4)}} = i^m \tag{22}$$

Finally, by simple geometrical considerations it can easily be proved that $\psi^i = \psi^r = \psi$ and $\sqrt{(D/R^{i,r})} \mathrm{e}^{-\mathrm{i}k_s (D - R^{i,r})} \cong \mathrm{e}^{-\mathrm{i}k_s (L \cos\psi \mp H \sin\psi)}$ for $D \to \infty$, such that Equation (20) becomes:

$$w^{(0)}|_{cyl} \cong \mathrm{e}^{-\mathrm{i}k_s L \cos\psi} \left\{ \mathrm{e}^{\mathrm{i}k_s H \sin\psi} \sum_{m=0}^{+\infty} \varepsilon_m (-\mathrm{i})^m J_m \cos m(\theta_2 - \psi) + \mathrm{e}^{-\mathrm{i}k_s H \sin\psi} \sum_{m=0}^{+\infty} \varepsilon_m (-\mathrm{i})^m J_m \cos m(\theta_2 + \psi) \right\} \tag{23}$$

Notice that Equation (23) is the same as Equation (9). This suggests that taking into account the normalization of the cylindrical free-field solution, with respect to an appropriate function, allows

DOI: 10.1002/eqe

one to describe the limiting condition that, for sufficiently large source–receiver distance, harmonic cylindrical waves are reduced to plane waves. It was found that, as a rule of thumb, this occurs for dominant wavelengths larger than the cavity size, when the source-to-site distance is greater than about 20 times the radius of the cavity.

NUMERICAL RESULTS

Some numerical results of potential practical interest are illustrated here, with reference to the incidence of plane waves in the presence of underground cavities. First, the analytical solutions for both cavities and elastic inclusions are shown in time and frequency domains as a function of normalized dimensionless quantities. After that, the transfer function for surface ground motion above underground cavities is analyzed in more detail, focusing on the physical interpretation of its fundamental frequency and its higher harmonics, using the Rayleigh's method to geological structures is shown. Finally, we provide quantitative estimates of the amplification of surface ground motion above underground cavities, based on response spectra of real accelerograms, for some representative cases of practical interest.

Synthetic seismograms and transfer functions

To provide insights into the physics of the problem, Figure 3 illustrates some examples of synthetic seismograms for the cases of: (a) a cavity; (b) a lined tunnel having a circular boundary with properties $b=0.125, \beta_c/\beta_s=2.5, \rho_c/\rho_s=1.5$ and (c) an elastic inclusion with $\beta_c/\beta_s=2.5$ and $\rho_c/\rho_s=1.5$. Results refer to both plane (top panel) and cylindrical (bottom panel) waves, assuming vertical incidence ($\psi=90°$). For the three cases, the cavity/inclusion has a unit radius a_c and an embedment depth $H=3a_c$. Furthermore, a dimensionless frequency is introduced as the ratio of the diameter of the inclusion to the wavelength:

$$\eta=\frac{\omega}{\pi}\frac{a_c}{\beta_s}=\frac{2a_c}{\lambda} \tag{24}$$

Note that in absence of the underground structure, the amplitude of surface ground motion is assumed to be 1 (i.e. free-field solution). Because of the small propagation distances involved, the dependence of results on the quality factor Q is negligible. For this reason, $Q=1000$ has been considered throughout this study.

In this example the peak dimensionless frequency of the seismic excitation is selected to be close to 1. The seismograms have been computed by convolution of the analytical solutions with a Ricker wavelet, whose time dependence is given by the equation:

$$f(t)=[1-2\pi^2 f_p^2(t-t_0)^2]e^{-\pi^2 f_p^2(t-t_0)^2} \tag{25}$$

where f_p is the peak frequency of the Fourier amplitude spectrum and t_0 is the time shift parameter. The selected parameters are: $f_p=0.5\,\text{Hz}, t_0=4$ and 5 s, for plane and cylindrical waves incidence, respectively.

The most relevant phases of ground motions can be clearly detected on the top left-hand side of Figure 3: the direct arrival, denoted by D, the reflected phase (R) and some multiples (M_1 and M_2), corresponding to waves travelling along one quarter and the whole surface of the cavity, respectively. Receivers located above the cavity (a) on the ground surface detect a direct wave front

DOI: 10.1002/eqe

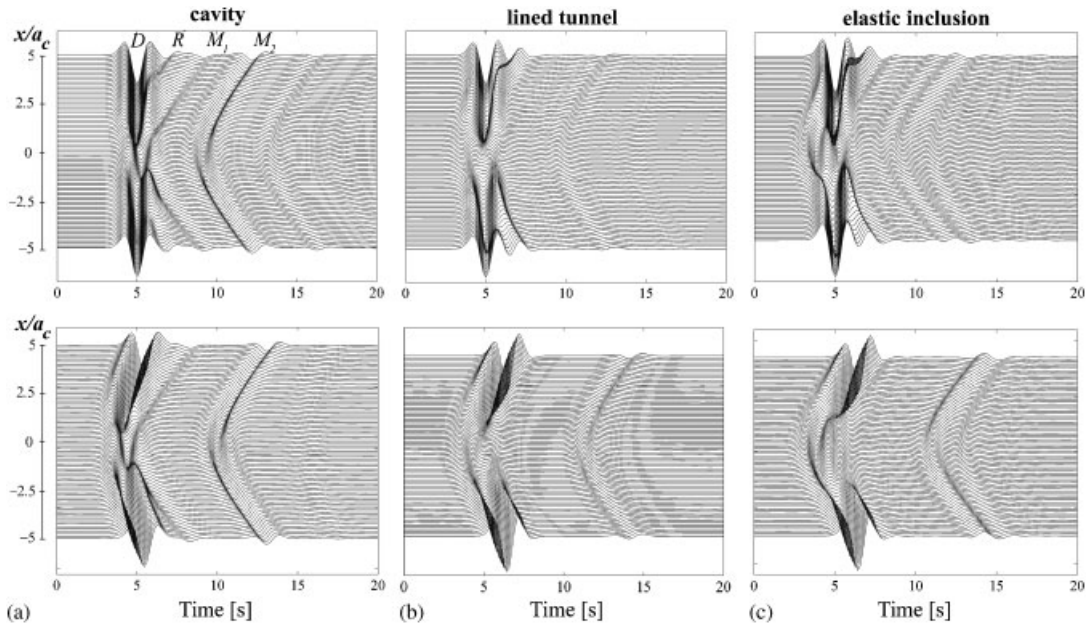

Figure 3. Synthetic seismograms obtained at 80 equally spaced receivers deployed along the ground surface for: (a) a cavity; (b) a cavity with a circular boundary of properties: $b=0.125$, $\beta_c/\beta_s=2.5$, $\rho_c/\rho_s=1.5$ and (c) an elastic inclusion with $\beta_c/\beta_s=2.5$, $\rho_c/\rho_s=1.5$ under plane (top panel) and cylindrical (bottom panel) waves incidence. For the three cases, the burial depth is $H=3a_c$. The most relevant phases of motion are superimposed on the left-hand side top graph: direct (D), reflected (R) and some multiples (M_1 and M_2).

which is significantly attenuated, at least for the range of frequencies and the embedment ratio investigated in this example. On the other hand, for receivers located either above the tunnel (b) or the elastic inclusion (c), the refracted phase arrives about 2 s before the direct arrival, owing to the higher S wave velocity within the inclusion. Note that the latter effect is more pronounced when the incident wavefield is represented by a nearby punctual source due to the intrinsic curvature of the incoming wave front.

Figure 4 compares the transfer functions at (a) $x/a_c=0$ and (b) $x/a_c=1$ for the same case studies illustrated in Figure 3. The transfer function of a cavity shows several peaks larger than 1 at nearly regularly spaced frequencies (this aspect will be discussed in the following section), while the presence of either a lined tunnel or an elastic inclusion filled with stiffer material with respect to the surrounding medium ($\beta_c/\beta_s=2.5$) induces a rather significant de-amplification of surface ground motions, at least for the considered range of frequencies and under the incidence of vertical plane waves.

Physical interpretation of ground motion harmonics

As a further example of the frequency dependence of our results, Figure 5 illustrates the modulus of the transfer function associated to an embedded shallow cavity with $a_c=5\,\mathrm{m}$, $H=8\,\mathrm{m}$, $\beta_s=200\,\mathrm{m/s}$ and $\rho_s=2000\,\mathrm{kg/m^3}$ subjected to incident vertical plane waves. Results for three representative positions along the ground surface, specifically (i) $x/a_c=0$, (ii) $x/a_c=1$ and (iii) $x/a_c=2$, are

DOI: 10.1002/eqe

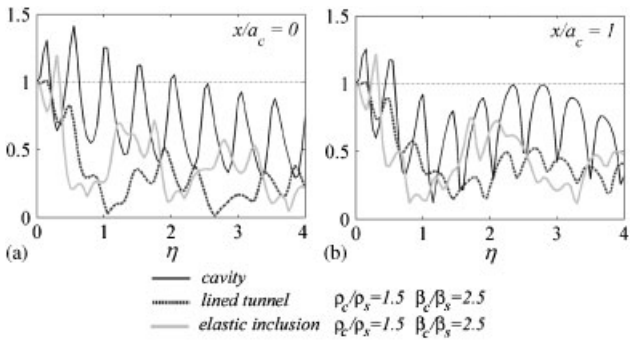

Figure 4. Comparison of the transfer functions at (a) $x/a_c = 0$ and (b) $x/a_c = 1$ for the same case studies illustrated in Figure 3. The incident wavefield is given by vertically propagating plane waves.

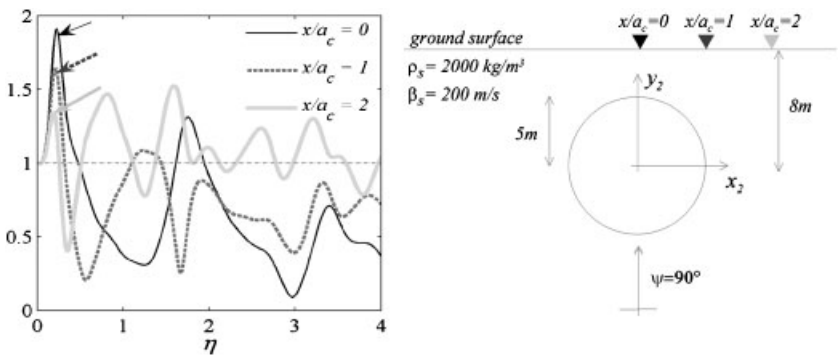

Figure 5. Absolute value of the transfer function of a shallow cavity in terms of the normalized frequency η at three representative observation points located at: (i) $x/a_c = 0$; (ii) $x/a_c = 1$ and (iii) $x/a_c = 2$. The superimposed arrows on the left-hand side indicate the peak associated with the fundamental vibration mode. The properties of the model under study are reported in the right-hand side sketch.

compared. Leaving aside for the moment the higher harmonics, which will be analyzed in the sequel, we address now the interpretation of the first peak shown by an arrow in Figure 5. The observation that such peak appears at the same frequency for all positions ranging from about $-3a_c$ to $+3a_c$ suggests that it corresponds to a vibration mode of a bounded portion of soil. To support the latter conjecture, we compared the fundamental frequency corresponding to such peak with the one estimated by a simple application of the Rayleigh's method. For a thorough discussion of this method applied to geological structures, we refer the reader to Dobry *et al.* [19] and Paolucci [20, 21].

The starting point of the method is the assumption of a suitable approximation of the actual mode shape $\overline{\phi}_z(x, y)$ (along the z-direction) under SH wave propagation, so that the fundamental vibration frequency can be bounded as:

$$\omega_0^2 \leqslant \min_{\phi_z} \frac{\int_\Omega \sigma_{ij}(x, y)\varepsilon_{ij}(x, y)\, d\Omega}{\int_\Omega \rho(x, y)\phi_z^2(x, y)\, d\Omega} \tag{26}$$

DOI: 10.1002/eqe

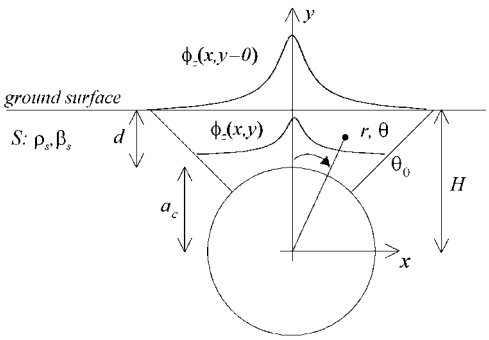

Figure 6. Geometry of the model under study and polar reference system used for the application of the Rayleigh's method. Superimposed in the (x, y) plane are two idealized profiles, at ground surface and at a given depth, of the mode of vibration $\phi_z(x, y)$ of the portion of soil of thickness d.

where $\sigma_{ij}(x, y)$ is the stress tensor computed by Hooke's law, $\varepsilon_{ij}(x, y)$ is the strain tensor and $\phi_z(x, y)$ is an admissible (i.e. satisfying the boundary conditions) approximation of the mode shape $\overline{\phi}_z(x, y)$. Equation (26) follows by equating the elastic strain energy and the kinetic energy of the vibrating bounded medium, defined in the spatial domain Ω.

The geometry and the polar reference system referred to for the application of the Rayleigh's method are sketched in Figure 6. The domain Ω of existence of the proposed mode shape $\phi_z(x, y)$ is constrained laterally by radial segments of inclination θ_0. In a polar reference system (r, θ) with origin in the center of the cavity (see Figure 6) the following expression for $\phi_z(r, \theta)$ is assumed:

$$\phi_z(r,\theta) = \left(\frac{r}{H}\right)^m \cos^s\left(\frac{\pi\theta}{2\theta_0}\right) \tag{27}$$

where m, s and θ_0 are parameters to be obtained through a minimization process. As an illustrative example, two idealized profiles, at ground surface and at a given depth, of the mode of vibration $\phi_z(x, y)$ are shown in Figure 6.

Under SH wave propagation, the non-vanishing components of the strain tensor are given by:

$$\gamma_{rz}(r,\theta) = \frac{\partial\phi_z}{\partial r}(r,\theta) = H^{-m} m r^{m-1} \cos^s\left(\frac{\pi\theta}{2\theta_0}\right) \tag{28a}$$

$$\gamma_{\theta z}(r,\theta) = \frac{1}{r}\frac{\partial\phi_z}{\partial\vartheta}(r,\vartheta) = -\frac{\pi}{2\theta_0}\frac{r^{m-1}}{H^m} s \cos^{s-1}\left(\frac{\pi\theta}{2\theta_0}\right)\sin\left(\frac{\pi\theta}{2\theta_0}\right) \tag{28b}$$

such that Equation (26) specializes as follows:

$$\omega_0^2 \leqslant \min_{s,m,\theta_0} \frac{\int_\Omega \mu(\gamma_{rz}^2+\gamma_{\theta z}^2)\,\mathrm{d}\Omega}{\int_\Omega \rho\phi_z^2\,\mathrm{d}\Omega} = \min_{s,m,\theta_0}\left\{\beta^2\frac{I_1}{I_2}\right\} \tag{29}$$

DOI: 10.1002/eqe

with

$$I_1 = \int_0^{\theta_0} \int_a^{H/\cos\theta} \left\{ \left[m \frac{r^{m-1}}{H^m} \cos^s\left(\frac{\pi\theta}{2\theta_0}\right) \right]^2 + \left[\frac{\pi}{2\theta_0} \frac{r^{m-1}}{H^m} s \cos^{s-1}\left(\frac{\pi\theta}{2\theta_0}\right) \sin\left(\frac{\pi\theta}{2\theta_0}\right) \right]^2 \right\} r \, \mathrm{d}r \, \mathrm{d}\theta \tag{30a}$$

$$I_2 = \int_0^{\theta_0} \int_a^{H/\cos\theta} \left[\frac{\pi}{2\theta_0} \frac{r^{m-1}}{H^m} s \cos^{s-1}\left(\frac{\pi\theta}{2\theta_0}\right) \sin\left(\frac{\pi\theta}{2\theta_0}\right) \right]^2 r \, \mathrm{d}r \, \mathrm{d}\theta \tag{30b}$$

calculated numerically with Gaussian quadrature formulas. The fundamental frequency is found by a standard minimization procedure with respect to the parameters m, s and θ_0.

Figure 7 compares the analytical fundamental vibration frequency, denoted as η_p from here on, and the values estimated by the application of Rayleigh's method as a function of the ratio of the embedment depth H over the radius of the cavity a_c. It is worth underlining that this was found to be the only parameter controlling η_p. Attention is limited herein to the transfer function computed at $x/a_c = 0$. The good agreement between the actual fundamental frequency and that estimated by Rayleigh's method (as expected from the well-known property of Rayleigh's quotient, the estimated value is larger than the analytical one) strongly supports the hypothesis of a fundamental vibration mode which dominates surface ground motions at low dimensionless frequencies. The fundamental mode shape turns out to be defined typically by values of $\theta_0 \sim$ 80–85°, $s \sim$1.1–1.3 and $m \sim$0.1–0.2. The large values of θ_0, combined with the values of s strictly larger than 1, indicate that significant amplification (>10%) of motion at ground surface may reach an extent up to approximately $\pm 5a_c$, while the low values of m point out a tiny attenuation of the fundamental mode shape with depth within the domain of interest. These results have been confirmed by numerical simulations as well, not shown here for brevity.

Another interesting result is that the computed pairs $(\eta_p, H/a_c)$ turn out to be approximated with reasonable accuracy by a curve of equation:

$$\eta_p \approx \tfrac{1}{3} \cdot (H/a_c)^{-1} \tag{31}$$

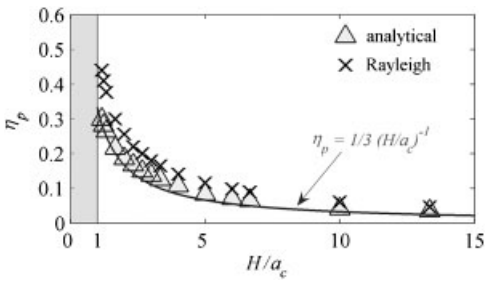

Figure 7. Dimensionless fundamental vibration frequency η_p as a function of the ratio H/a_c. The computed analytical values (filled triangles) are compared with the estimates by Rayleigh's method (crosses).

DOI: 10.1002/eqe

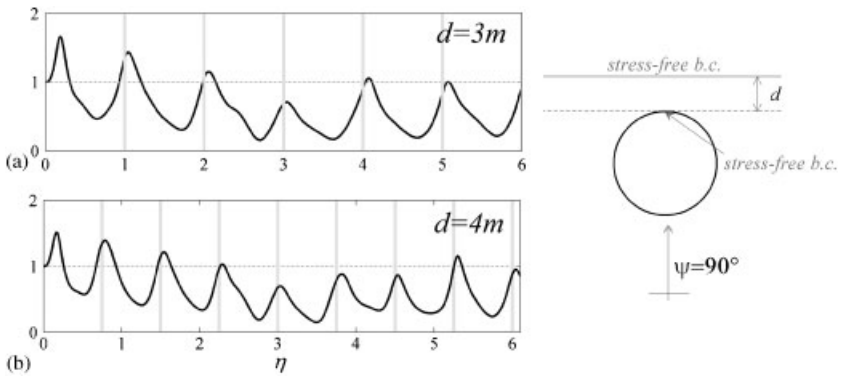

Figure 8. Transfer functions computed at $x/a_c=0$ for the following cases: (a) $H/a_c=2$ and (b) $H/a_c=\frac{7}{3}$. The vertical gray lines superimposed on the left-hand side point out the natural frequencies of a free–free plate of thickness d, given by Equation (33).

to be obviously applied for $H/a_c>1.0$. From Equations (31), it follows that the wavelength λ_p, associated with the fundamental vibration mode, can be roughly estimated as:

$$\lambda_p \approx 6H \tag{32}$$

The dominant wavelength of surface ground motion above underground cavities turns out to depend only on the geometry of the problem, and it is equal to about 6 times the embedment depth.

We touch now on the issue regarding the physical interpretation of the higher harmonics of the transfer function at $x/a_c=0$ associated with buried cavities under vertical plane incidence. These harmonics were found to coincide with the modal vibration frequencies of a plate of thickness d with free–free boundary conditions, given by the following expression:

$$\eta_n = n\frac{a_c}{d} \quad \text{with } n \geqslant 1 \tag{33}$$

To support this finding, Figure 8 shows the transfer functions (left-hand side) computed at $x/a_c=0$ for two different configurations, namely: (a) $H/a_c=2$ and (b) $H/a_c=7/3$ (see sketches on the right-hand side). It is apparent that the higher harmonics have natural frequencies that are in good agreement with the assumed model.

Quantification of the effect of underground cavities on surface ground motion, based on real accelerograms

To summarize the previous analytical findings, we provide in this section an example of the practical quantification of the effect of underground cavities on surface ground motion based on real accelerograms. Specifically, the procedure devised herein is the following. For a set of representative configurations, in terms of radius size, embedment depth and dynamic properties of the halfspace, an appropriate suite of output accelerograms was obtained by convolving the surface response at selected receivers with a representative set of seven real accelerograms. These accelerograms, reported in Table I, belong to an ensemble selected to fit, on average, the EC8 response spectral shape for stiff soil conditions, with anchor acceleration at zero period $a_g=0.25g$ (Lai, 2007; Pers. Comm.).

DOI: 10.1002/eqe

Table I. Details about the suite of real accelerograms considered for computing average amplification factors for elastic response spectra; R = epicentral distance, M_W = moment magnitude, and PGA = peak ground acceleration.

Event name	Date	R (km)	M_W	PGA (g)
Friuli (aftershock)	09/11/1976	16	5.6	0.23
Montenegro	04/15/1979	16	7.0	0.36
Kalamata (Southern Greece)	09/13/1986	10	5.8	0.24
Erzincan (Turkey)	03/13/1992	13	6.7	0.39
Ionian (Greece)	03/23/1983	18	6.2	0.23
Parkfield	09/28/2004	11.6	6.0	0.30
Parkfield	09/28/2004	14	6.0	0.24

After convolution, the 5% damped acceleration response spectrum (SA) of each accelerogram was divided by the corresponding SA of the input accelerogram. Subsequently, the average ($\pm 1\sigma$) ratios $R_{\mathrm{SA}}(T)$ of output vs input SA over the considered suite of accelerograms were calculated. The covariance coefficient was found to range from 5 to 15%, approximately.

As an illustrative example, Figure 9 depicts variations of the spectral amplification factor $R_{\mathrm{SA}}(T)$ (black lines) calculated at positions $x/a_{\mathrm{c}} = 0, 1, 2$ and 5, under vertical plane incidence, when two representative cavities are considered: (a) $H = 8\,\mathrm{m}$, $a_{\mathrm{c}} = 4\,\mathrm{m}$ and $\beta_{\mathrm{s}} = 500\,\mathrm{m/s}$ (left) and (b) $H = 15\,\mathrm{m}, a_{\mathrm{c}} = 3\,\mathrm{m}$ and $\beta_{\mathrm{s}} = 400\,\mathrm{m/s}$ (right). In each case, $\rho_{\mathrm{s}} = 2000\,\mathrm{kg/m^3}$, value that will be understood in the sequel. The dispersion of the curves ($\pm 1\sigma$) is also shown by thin gray lines, indicating a not negligible dependence of $R_{\mathrm{SA}}(T)$ on the input ground motion, especially at very low periods. Nonetheless, from here on, we will refer to the average ratios for the sake of simplicity, keeping in mind that a maximum deviation of around 15% of the mean could apply. As expected, significant variations of $R_{\mathrm{SA}}(T)$ with respect to unity are limited to $|x/a_{\mathrm{c}}| < 5$. The largest values of $R_{\mathrm{SA}}(T)$ occur at $x/a_{\mathrm{c}} = 0$, exactly at top of the cavity along the ground surface, while $R_{\mathrm{SA}}(T) < 1.1$ for $|x/a_{\mathrm{c}}| > 5$. The maximum $R_{\mathrm{SA}}(T)$ ranges from about 1.4 to 1.25, passing from (a) to (b), in the period range from approximately 0.1 to 0.2 s. Recalling the definition of η (see Equation (24)), according to Equation (31), the structural period mostly affected by the presence of underground cavities can be roughly estimated as:

$$T_p = \frac{2a_{\mathrm{c}}}{\beta_{\mathrm{s}}} \frac{1}{\eta_p} \approx 6\frac{H}{\beta_{\mathrm{s}}} \tag{34}$$

Considering realistic values of H and β_{s}, the presence of underground cavities is expected to induce significant effects on surface ground motion limited to the low period branches of the acceleration response spectra. Taking, for instance, $H = 15\,\mathrm{m}$ and $\beta_{\mathrm{s}} = 400\,\mathrm{m/s}$ as representative values, $T_p \sim 0.2\,\mathrm{s}$ is obtained, and the effects for longer periods will be negligible.

Equation (34) suggests a way of representing the average ratios as a function of a dimensionless period defined as follows:

$$T^{\mathrm{N}} = \frac{T\beta_{\mathrm{s}}}{H} \tag{35}$$

Figure 10 shows the variations of the amplification factor $R_{\mathrm{SA}}(T^{\mathrm{N}})$ for different values of the embedment ratio H/a_{c} and normalized distance x/a_{c} ($\beta_{\mathrm{s}} = 400\,\mathrm{m/s}$ and $\rho_{\mathrm{s}} = 2000\,\mathrm{kg/m^3}$). Results for six representative values of the dimensionless depth H/a_{c} (from 1.5 to 5.0) over the distance

DOI: 10.1002/eqe

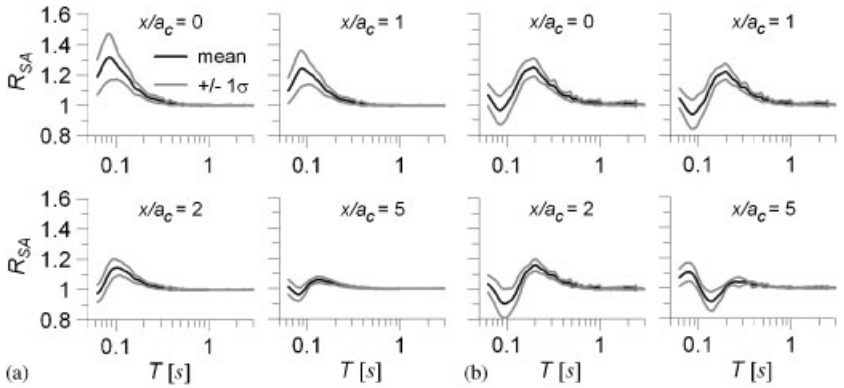

Figure 9. Average ratios (black lines) and $\pm 1\sigma$ (gray lines) of output over input acceleration response spectra (at 5% damping) at different positions x/a_c when two representative cavities are considered: (a) $H/a_c = 2, \beta_s = 500\,\mathrm{m/s}, \rho_s = 2000\,\mathrm{kg/m^3}$ (left) and (b) $H/a_c = 3, \beta_s = 400\,\mathrm{m/s}, \rho_s = 2000\,\mathrm{kg/m^3}$ (right).

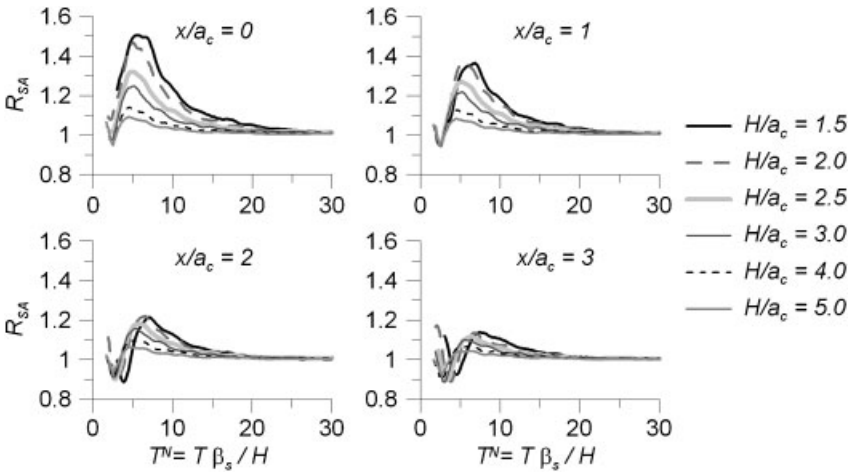

Figure 10. Amplification factors on acceleration response spectra, R_{SA}, as a function of the normalized period $T^N = T\beta_s/H$, for increasing values of H/a_c and for various dimensionless distances. For the half-space, $\beta_s = 400\,\mathrm{m/s}$ and $\rho_s = 2000\,\mathrm{kg/m^3}$ were considered. Results refer here to vertical plane waves incidence, condition for which the most significant effects are found.

range $|x/a_c| \leqslant 3$ are shown; larger distances are omitted because the corresponding amplification factors are of little engineering interest ($<1.1\%$). It is apparent that, thanks to the normalization, all response ratios R_{SA} peak around $T^N = 6$, supporting Equation (34), but their amplitudes strongly depend on the parameters H/a_c and x/a_c with decreasing values of R_{SA} with H/a_c and x/a_c, as expected. A slight increasing trend of the amplified periods is noted for increasing values of x/a_c, but this effect can reasonably be neglected from a practical point of view. Significant values of R_{SA} above unity are noted typically for $H/a_c < 3$, while for larger values the spectral amplification factor tends to be smaller than about 1.1–1.2. The maximum value of R_{SA}, around 1.5, is found

DOI: 10.1002/eqe

for $H/a_c = 1.5$ and $x/a_c = 0$, i.e. above a shallow cavity with large diameter. Furthermore, even though not shown here for brevity, it is noted that the peak values of R_{SA} tend to increase when softer media are considered (a maximum increase of $\sim 20\%$ is observed passing from $\beta_s = 600$ to 200 m/s). Nevertheless, such an effect is notable only for values of $H/a_c < 2$, thus confirming that the geometry is the key factor that controls the observed amplification. Finally, note that the results in Figure 10 are based on vertical plane wave incidence, when the most critical amplification factors are obtained. Even though not shown here for brevity, we have verified that oblique incidence induces a significant reduction of the amplification factor (e.g. for $H/a_c = 2$ and $x/a_c = 0$, R_{SA} decreases by about 20% passing from $\psi = 90°$ to $\psi = 30°$) since the fundamental vibration mode is no longer fully excited.

CONCLUSIONS

Several analytical solutions have been presented to study the antiplane seismic response of various types of underground structures, from cylindrical cavities, to tunnels up to inclusions filled in with material of arbitrary rigidity, subjected to either plane or cylindrical waves. The method of solution is based on the expansion of wave functions in terms of Bessel's and Hankel's functions, and their transport within a suitable set of cylindrical coordinate systems is obtained thanks to the application of Graf's addition theorem. The same tool, accompanied by an appropriate normalization process, allows us to derive the exact asymptotic equivalence, at large source–receiver distances, between wavefields at ground surface induced by plane and cylindrical waves. Indeed, the proposed method of solution turns out to be versatile in dealing both with different kinds of inclusions, and different types of incident wavefields as well.

Among the broad set of analytical solutions that could be obtained through the proposed method, particular emphasis was given to the physical interpretation of the transfer function of surface ground motion above underground cavities, under vertically incident plane waves. To this end, a simple application of the Rayleigh's method was carried out confirming that surface ground motions are controlled by the antiplane vibration modes of the portion of soil between the cavity and surface, in the range of frequencies of interest for engineering purposes. An approximate relationship for the fundamental vibration frequency as a function of the ratio of the embedment depth H to the radius of the cavity a_c has been obtained and provides a rough estimate of the fundamental frequencies. According to this simple formula, it turns out that the dominant wavelength associated with the fundamental vibration mode is about 6 times the embedment depth.

To provide quantitative estimates of the effect of underground cavities on surface ground motion, spectral amplification factors R_{SA} are computed as the average ratio of the output to the input acceleration response spectra. The interesting feature of such factors is that they can be expressed as a function of the dimensionless period $T^N = T\beta_s/H$ for a set of representative real cases. The obtained amplification factors tend to peak at $T^N \sim 6$ with values up to about 1.5, for $x/a_c = 0$, $H/a_c = 1.5$–2.0 and vertical plane incidence. It is found that the most critical amplification factors are obtained for vertical or nearly vertical wave incidence, when the fundamental vibration mode is fully excited. As a practical indication, R_{SA} is significantly larger than 1 for $H/a_c \leqslant 3$ and distances $|x/a_c| \leqslant 3$, approximately, while for larger embedment ratios and distances, it tends to unity. Based on the previous results and on realistic values of the input parameters, both in terms of seismic input and soil dynamic properties, it can be deduced that the presence of buried cavities is expected to induce significant effects limited to the low period ranges of the acceleration response

DOI: 10.1002/eqe

spectrum, typically within structural periods varying from 0.05 to 0.2 s, with spectral amplification factors up to about 1.5. As a concluding remark, it is worth underlining that the results of this paper are limited to the case of SH wave propagation. Preliminary findings, based on numerical simulations under SV-P wave incidence, show that the largest levels of amplification may occur at larger distance from the cavity, specifically at $x/a_c \sim 3$, where the maximum of the in-plane vibration mode is supposed to occur.

APPENDIX A: GRAF'S ADDITION THEOREM FOR WAVE PROPAGATION ANALYSES

We illustrate here a generalized version of Graf's addition theorem, easy to specialize to different kinds of applications of seismic wave propagation in elastic media.

Given the set of reference system sketched in Figure A1, the scope is to express an arbitrary wave solution, originally given with respect to the system centered in B, in terms of the radial coordinates of the system centered in A. For instance, provided the wave solution in terms of $H_m^{(2)}(k|x-y|)$ and ϕ, we seek the equivalent solution in terms of the polar coordinates $(|y|, \vartheta_y)$. Applying the definition of Graf's addition theorem as provided by Abramowitz and Stegun [14] we end up with the following compact expression:

$$H_m^{(2)}(k|x-y|)\mathrm{e}^{\mathrm{i}m\phi} = \sum_{n=-\infty}^{+\infty} H_{m+n}^{(2)}(kr_>)\mathrm{e}^{\mathrm{i}(m+n)\vartheta_x} J_n(kr_<)\mathrm{e}^{-\mathrm{i}n\vartheta_y} \tag{A1}$$

where $r_> = \max\{|x|, |y|\}$ and $r_< = \min\{|x|, |y|\}$.

For ease of notation, let us define the following quantities: $H_m \equiv H_m^{(2)}(k|x-y|)$; $H_{m\pm n} \equiv H_{m\pm n}^{(2)}(kr_>)$ and $J_n \equiv J_n(kr_<)$. Expanding Equation (A1) with Euler's formula and factorizing with respect to the real and imaginary parts, we obtain the following expressions, respectively:

$$\begin{aligned} H_m \cos m\phi = &\sum_{n=0}^{+\infty} \frac{\varepsilon_n}{2}\{H_{m+n}\cos[(m+n)\vartheta_x] + (-1)^n H_{m-n}\cos[(m-n)\vartheta_x]\} J_n \cos n\vartheta_y \\ &+ \sum_{n=1}^{+\infty}\{H_{m+n}\sin[(m+n)\vartheta_x] - (-1)^n H_{m-n}\sin[(m-n)\vartheta_x]\} J_n \sin n\vartheta_y \end{aligned} \tag{A2}$$

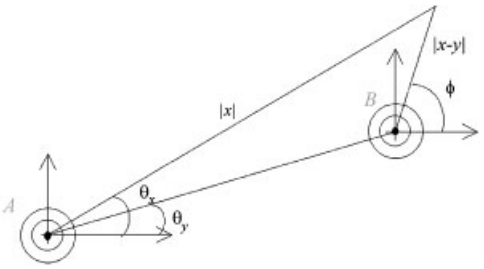

Figure A1. Set of reference systems referred to in the text for the application of Graf's addition theorem.

DOI: 10.1002/eqe

$$H_m \sin m\phi = \sum_{n=0}^{+\infty} \frac{\varepsilon_n}{2} \{H_{m+n} \sin[(m+n)\vartheta_x] + (-1)^n H_{m-n} \sin[(m-n)\vartheta_x]\} J_n \cos n\vartheta y$$
$$- \sum_{n=1}^{+\infty} \{H_{m+n} \cos[(m+n)\vartheta_x] - (-1)^n H_{m-n} \cos[(m-n)\vartheta_x]\} J_n \sin n\vartheta y \quad \text{(A3)}$$

Defining the transport factors $K_{mn}^{\pm}$ and $L_{mn}^{\pm}$ as follows:

$$K_{mn}^{\pm} = \{H_{m+n} \cos[(m+n)\vartheta_x] \pm (-1)^n H_{m-n} \cos[(m-n)\vartheta_x]\} \quad \text{(A4a)}$$

$$L_{mn}^{\pm} = \{H_{m+n} \sin[(m+n)\vartheta_x] \pm (-1)^n H_{m-n} \sin[(m-n)\vartheta_x]\} \quad \text{(A4b)}$$

it is easy to verify the following identities:

$$H_m \cos m\phi = \sum_{n=0}^{+\infty} J_n \left[\frac{\varepsilon_n}{2} K_{mn}^{+} \cos n\vartheta_y + \hat{\delta}_{n0} L_{mn}^{-} \sin n\vartheta_y \right] \quad \text{(A5a)}$$

$$H_m \sin m\phi = \sum_{n=0}^{+\infty} J_n \left[\frac{\varepsilon_n}{2} L_{mn}^{+} \cos n\vartheta_y - \hat{\delta}_{n0} K_{mn}^{-} \sin n\vartheta_y \right] \quad \text{(A5b)}$$

ACKNOWLEDGEMENTS

This work was done while the first author (C. S.) was on leave from the ROSE School, of Pavia, Italy, at the Institute of Engineering of UNAM, Mexico. G. Sánchez N. and her team of Unidad de Servicios de Información (USI) helped us with useful references. Partial support from DGAPA-UNAM, Mexico, under Project IN114706 is gratefully acknowledged as well as from the Department of Civil Protection (DPC) of Italian Government within the framework of '*RELUIS-DPC—Linea di Ricerca n. 6— Geotecnica Sismica—Costruzioni in Sotterraneo, Gallerie e Caverne in Roccia*'. Comments of two anonymous reviewers are also kindly acknowledged.

REFERENCES

1. CEN Eurocode 8—design of structures for earthquake resistance. *Part 5*: *Foundations, Retaining Structures and Geotechnical Aspects*, *prEN 1998-5*. Comité Européen de Normalisation, Brussels, 2006.
2. Pao HY, Mow CC. *The Diffraction of Elastic Waves and Dynamic Stress Concentrations*. Crane-Russak: New York, 1973.
3. Datta SK, El-Akily N. Diffraction of elastic waves by cylindrical cavity in a half-space. *Journal of the Acoustical Society of America* 1978; **64**(6):1692–1978.
4. Wong KC, Shah AH, Datta SK. Diffraction of elastic waves in a half-space, II. Analytical and numerical solutions. *Bulletin of the Seismological Society of America* 1985; **75**(1):69–92.
5. Dravinski M. Scattering of SH waves by subsurface topography. *Journal of the Engineering Mechanics Division* (ASCE) 1982; **108**(1):1–17.
6. Dravinski M. Ground motion amplification due to elastic inclusions in a halfspace. *Earthquake Engineering and Structural Dynamics* 1983; **11**(3):313–335.
7. Lee VW. On deformations near circular underground cavity subjected to incident plane SH waves. *Proceedings Symposium of Applications of Computer Methods in Engineering*, USC, Los Angeles, 1977; 951–961.
8. Lee VW, Trifunac MD. Response of tunnels to incident SH-waves. *Journal of the Engineering Mechanics Division* (ASCE) 1979: **105**(4):643–659.
9. Lee VW. Three-dimensional diffraction of elastic waves by a spherical cavity in an elastic halfspace, I: closed-form solutions. *Soil Dynamics and Earthquake Engineering* 1988; **7**(3):149–161.

DOI: 10.1002/eqe

10. Lee VW, Karl J. Diffraction of SV waves by underground, circular, cylindrical cavities. *Soil Dynamics and Earthquake Engineering* 1992; **11**(8):445–456.
11. Lee VW, Karl J. Diffraction of elastic plane P waves by circular, underground unlined tunnels. *European Earthquake Engineering* 1993; **6**(1):29–36.
12. Lee VW, Chen S, Hsu IR. Antiplane diffraction from canyon above subsurface unlined tunnel. *Journal of Engineering Mechanics* 1999; **125**(6):668–675.
13. Avilés J, Mora-Orozco LS. Modificación del movimiento sísmico por obstrucciones subterráneas. *Sismodinámica* 1990; **1**(3):147–170.
14. Abramowitz M, Stegun IA. *Handbook of Mathematical Functions*. National Bureau of Standards: Washington, DC, 1964.
15. Avilés J, Sánchez-Sesma FJ. Piles as barriers for elastic waves. *Journal of Geotechnical Engineering* 1983; **109**(9):1133–1146.
16. Lee VW, Manoogian ME, Chen S. Anti-plane SH deformations near a surface rigid foundation above a subsurface rigid circular tunnel. *Earthquake Engineering and Engineering Vibration* 2002; **1**(1):27–35.
17. Achenbach JD. *Wave Propagation in Elastic Solids*. North-Holland Publishing Co.: Amsterdam, 1973.
18. Sommerfeld A. *Partial Differential Equations in Physics*. Academic Press Inc.: New York, 1949.
19. Dobry RI, Oweis I, Urzua A. Simplified procedures for estimating the fundamental period of a soil profile. *Bulletin of the Seismological Society of America* 1976; **66**:1293–1321.
20. Paolucci R. Shear resonance frequencies of alluvial valleys by Rayleigh's method. *Earthquake Spectra* 1999; **15**(3):503–521.
21. Paolucci R. Amplification of earthquake ground motion by steep topographic irregularities. *Earthquake Engineering and Structural Dynamics* 2002; **31**:1831–1853. DOI: 10.1002/eqe.192.